



# Design, Synthesis, and Fabrication of Chitosan/Hydroxyapatite Composite Scaffold for Use as Bone Replacement Tissue by Sol–Gel Method

Ashkan Farazin<sup>1</sup> · Amir Hossein Ghasemi<sup>2</sup>

Received: 9 February 2022 / Accepted: 5 April 2022 / Published online: 19 April 2022

© The Author(s), under exclusive licence to Springer Science+Business Media, LLC, part of Springer Nature 2022

## Abstract

Injuries or bone defects are phenomena that are harmful to human health. In the field of bone scaffold tissue engineering, hydroxyapatite nanoparticles have been considered due to their high similarity to inorganic bone composition, but despite the similarity of chemical composition, the mechanical properties of synthetic hydroxyapatite (HA) are weak compared to bone. In this study, hydroxyapatite nanoparticles were synthesized by the sol–gel method. Then eight samples of composite scaffolds with chitosan (Chi) as biopolymer and different percentages of hydroxyapatite (0, 25, 50, and 75%) were prepared using a crosslinker of glutaraldehyde (GA) and sodium tripolyphosphate (TPP). To characterize the synthesized hydroxyapatite powder and scaffold samples, FTIR, FE-SEM, XRD, DTA-TG characterization tests, bioactivity analysis, and also strength test were performed. The results of the FESEM analysis show that hydroxyapatite particles with an average size of 48 nm have been synthesized by the sol–gel method. Also, FE-SEM images of scaffold samples show that as the amount of hydroxyapatite increases, the size of the pores decreases, and their distribution is uniform. FTIR spectroscopic analysis shows that both types of crosslinkers behave almost similarly and that the hydroxyapatite particles have established hydrogen bonds with the chitosan. Samples containing 75 wt.% of hydroxyapatite have the highest compressive strength and samples containing 50 wt.% of hydroxyapatite have the best behavior in terms of elongation. Scaffold samples were placed in simulated body fluid (SBF) for biological analysis for 1 week. FESEM images after removal of scaffolds from SBF solution show that the amount of calcium and phosphate ions adsorbed on scaffold samples containing 75 wt.% of hydroxyapatite is higher than other samples. One of the most important results of glutaraldehyde cross-linking with hydroxyapatite is that it controls the mechanical properties and adsorption rate without reducing the high biocompatibility of the composite. Also in this study, CHI-HA50%-TPP scaffolds exhibited the most promising physiochemical and biocompatible properties which can be used as an alternative regenerative material for bone tissue engineering.

**Keywords** Bone scaffold · Hydroxyapatite · Biological analysis · Mechanical properties · Sol–gel method

## 1 Introduction

Tissue engineering is an interdisciplinary science that offers a new approach to repairing the body's natural tissues by applying the laws of engineering and biological sciences

[1–3]. In tissue engineering, the presence of a suitable bio-mimetic scaffold is essential for cell survival [4–6]. Scaffolds should provide the natural microenvironment around the cells and support cell adhesion, anchorage, proliferation, and cell migration [7, 8]. The elastic modulus of metals is higher than 100 GPa, which is much higher than the stiffness of dense bone [9]. The result of this high stiffness is the emergence of a stress protection phenomenon on the growing bone [10–14], which will lead to thinning of the new bone tissue and increase the likelihood of its re-failure [15–17]. Problems such as this have drawn the attention of many researchers to newer materials [18–22]. Thus, a new topic called bone tissue engineering was opened and new biomaterials were introduced to the medical community

✉ Ashkan Farazin  
a.farazin@grad.kashanu.ac.ir

<sup>1</sup> Department of Solid Mechanics, Faculty of Mechanical Engineering, University of Kashan, P.O. Box, 87317-53153 Kashan, Iran

<sup>2</sup> Department of Organic Chemistry, Faculty of Chemistry, University of Kashan, P.O. Box, 87317-51167 Kashan, Iran

for this purpose [23, 24]. In general, tissue engineering can be defined as the application of scientific principles to the design, construction, modification, growth, and survival of living tissues in the body, according to which the properties of a biomaterial are subject to changes that can form tissue or release mass [25, 26]. From the cells into the host body and eventually, lead to the formation of new tissue [27, 28]. Therefore, it can be said that the bone tissue engineering method is based on the use of degradable biomaterials and despite its diversity, often follows a general rule that the steps of building a scaffold or degradable carrier, loading cells, drugs, growth proteins, and in general factors including bone growth and ultimately effective implantation of the set in the desired position are included [29–31]. The porous scaffold inside the body begins to break down, and at the same time, the cells cultured inside the structure continue to grow and proliferate until it is eventually replaced by new bone tissue [32]. Wang et al. [33] investigated the effect of citric acid addition on the formation of hydroxyapatite in the sol–gel process. These researchers used  $P_2O_5$  and  $Ca(NO_3)_2$  as raw materials in their study. The citric acid in sol–gel reactions accelerates the process of converting Sol to gel. Liu et al. [34] and Kalita [35] produced nanometer-sized hydroxyapatite with a size of 8–10 nm by the sol–gel method. Varma et al. [36] synthesized hydroxyapatite nanoparticles by polymer combustion and self-combustion synthesis in new body solutions. Shih et al. [37] used hydrolysis to produce 20 nm hydroxyapatite particles. Chitosan and its derivatives have been extensively tested in medical engineering, the pharmaceutical industry, and tissue engineering for their biocompatibility, biodegradation, and bacterial growth inhibition properties. Chitosan-based scaffolds are reinforced with nano-components of hydroxyapatite, ceramic glass, silica, titania and zirconia [38–41]. Hydroxyapatite/chitosan composite is widely used in the treatment of bone defects due to its interconnected nature with natural bone composition, biocompatibility and hydroxyapatite as a biomaterial [42, 43]. Chitosan solution and hydroxyapatite are water-based. Therefore, the formed scaffolds do not remain stable in water after freezing and solvent drying and disperse [44]. To solve this problem, a suitable crosslinking chitosan solution should be added [45, 46]. hydroxyapatite cannot be used alone to treat all bone defects due to its fragility,

and it is necessary to use polymer composite to enhance its mechanical and bioactive properties. For this reason, in this study, we tried to synthesize a nano-hydroxyapatite/chitosan composite for use as a bone replacement tissue in the most optimal state (Similar to Merck Company). Another innovation of the paper was the effect of hydroxyapatite content on scaffolding and crosslinker of sodium triphosphate and glutaraldehyde on scaffolds, which was analyzed. Chitosan solution and hydroxyapatite are water-based. Therefore, the formed scaffolds do not remain stable in water after freeze-drying. To solve this problem, a suitable crosslinking chitosan solution should be added. One of the challenges of this research is the type and amount of crosslinkers suitable for improving the strength and stability of the scaffold. Another challenge is the optimal amount of hydroxyapatite nanoparticles to obtain the desired properties, which was discussed in this study. In this paper, the particle size (48 nm), compressive strength (75 wt.% of hydroxyapatite have the highest compressive strength), elongation (50 wt.% of hydroxyapatite have the best behavior in terms of elongation), increase in porosity (96–90%) also further porosity facilitates the formation of bone and accelerates the healing of damaged bone, and very uniform distribution of nanoparticles in the polymer are completely optimized compared to previous studies.

## 2 Experimental

### 2.1 Materials

Diammonium hydrogen phosphate, Calcium nitrate tetrahydrate, phosphate, ethanol, ammonia solution, chitosan (Chi), Acetic acid (AA), Glutaraldehyde (GA), and Sodium tripolyphosphate (TPP) for the synthesis of hydroxyapatite and bone scaffold were purchased from Sigma Aldrich and Merck Company. Consumables for the synthesis of HA can be seen in Table 1 in detail.

### 2.2 Method of Synthesis of HA

First, 1 g of diammonium hydrogen phosphate in deionized water was stirred for 3 h by a magnetic stirrer. Then 2.98 g of

**Table 1** Consumables for the synthesis of HA

Material	Chemical formula	CAS registry number	Molar mass (g/mol)	Company
Diammonium hydrogen phosphate	$(NH_4)_2(HPO_4)$	7783–28–0	132.06	Sigma Aldrich
Calcium nitrate tetrahydrate	$CaH_8N_2O_{10}$	13477–34–4	236.15	Sigma Aldrich
Phosphate	$PO_4^{3-}$	14265–44–2	94.9714	Sigma Aldrich
Ethanol	$C_2H_5OH$	64–17–5	46.07	Sigma Aldrich-Merck
Ammonia solution	$NH_3$	664–41–7	17.03	Sigma Aldrich (14.5%)

calcium nitrate tetrahydrate in ethanol and deionized water (1:12) was stirred with a magnetic stirrer for 3 h (The pH of the solution was maintained between 10 and 12 by adding 14.5% ammonia solution). In the next step, diammonium hydrogen phosphate solution was added to the calcium nitrate tetrahydrate solution by burette. This step was performed in a low-temperature water bath (38–42 °C) for 4 h on a magnetic stirrer (400 rpm). The obtained material was filtered through filter paper and then washed several times with deionized water. The filtered material was placed in a dryer at 40 °C for 14 h. For complete drying, the sample was placed in a dryer at 60 °C for 2 h and placed at 80 °C for 18 h. The samples were then transferred to a furnace after drying. The sample temperature reached 700 °C at a rate of 10 °C/min and remained at 700 °C for 1 h until calcined hydroxyapatite powder was obtained.

### 2.3 Fabricating Bone Scaffold Samples

Consumables along with specifications for fabricating bone scaffolding can be seen in Table 2 in detail.

To investigate the effect of the amount of hydroxyapatite synthesized on the bone scaffold as well as the type of crosslinker, eight samples were prepared according to Table 3.

#### 2.3.1 Fabricating Chi/GA Sample

To fabricate a Chi/GA bone scaffold sample, first 0.05 g of low molecular weight chitosan powder was dissolved in 5 ml of 1% by volume acetic acid (1 wt.% chitosan) and placed on a magnetic stirrer for 2 min to obtain a clear gel. Then 0.5 ml of 1 wt.% glutaraldehyde was added to the formed gel and the obtained solution was placed on a magnetic stirrer for 3 h.

#### 2.3.2 Fabricating Chi/HA25%/GA Sample

To fabricate a Chi/HA25%/GA bone scaffold sample, first 0.15 g of low molecular weight chitosan powder was dissolved in 15 ml of acetic acid (1 wt.% chitosan) and stirred for 2 min by magnetic stirring to obtain a clear gel. Then 0.05 g of HA synthesized by sol–gel method was dispersed

**Table 3** Combination of samples made in this research

Sample name	Chitosan (wt.%)	Hydroxyapatite (wt.%)	Type of crosslinker
Chi/GA	100	0	GA
Chi/HA25%/GA	75	25	GA
Chi/HA50%/GA	50	50	GA
Chi/HA75%/GA	25	75	GA
Chi/TPP	100	0	TPP
Chi/HA25%/TPP	75	25	TPP
Chi/HA50%/TPP	50	50	TPP
Chi/HA75%/TPP	25	75	TPP

in some deionized water and the suspension obtained by burette was added to chitosan gel. It was then stirred by a magnetic stirrer for 2 h to obtain a (3:1 chitosan/hydroxyapatite solution). To the chitosan/hydroxyapatite solution, 1.5 ml of 1 wt.% glutaraldehyde was added and the resulting solution was placed on a magnetic stirrer for 3 h.

#### 2.3.3 Fabricating Chi/HA50%/GA Sample

To fabricate a Chi/HA50%/GA bone scaffold sample, first 0.15 g of low molecular weight chitosan powder was dissolved in 15 ml of 1% by volume acetic acid. It was then stirred by a magnetic stirrer for 2 min to obtain a clear gel. Then 0.15 g of HA synthesized by sol–gel method was dispersed in some deionized water and the suspension obtained by burette was added to chitosan gel. It was then stirred by a magnetic stirrer for 2 h to obtain a (1:1 chitosan/hydroxyapatite solution). To the chitosan/hydroxyapatite solution, 1.5 ml of 1 wt.% glutaraldehyde was added, and the obtained solution was placed on a magnetic stirrer for 3 h.

#### 2.3.4 Fabricating Chi/HA75%/GA Sample

To fabricate a Chi/HA75%/GA bone scaffold sample, the first 0.15 g of low molecular weight chitosan powder was dissolved in 15 ml of 1 wt.% acetic acid and stirred for 2 min by a magnetic stirrer to obtain a clear gel. Then 0.45 g of hydroxyapatite synthesized by sol–gel method was dispersed in some deionized water and the suspension

**Table 2** Consumables for fabricating bone scaffolding

Material	Chemical formula	CAS Registry Number	Molar mass (g/mol)	Company
Chitosan (3000 kDa)	(C <sub>6</sub> H <sub>11</sub> NO <sub>4</sub> ) <sub>n</sub>	9012–76–4	–	Merck
Acetic acid	CH <sub>3</sub> COOH	64–19–7	60.05	Sigma Aldrich
Glutaraldehyde	C <sub>5</sub> H <sub>8</sub> O <sub>2</sub>	111–30–8	100.11	Sigma Aldrich
Sodium triphosphate (15 wt.%)	Na <sub>5</sub> P <sub>3</sub> O <sub>10</sub>	7758–29–4	163.94	Sigma Aldrich

obtained by burette was added to chitosan gel. It was then stirred by a magnetic stirrer for 2 h to obtain a (1:3 chitosan/hydroxyapatite solution). To the chitosan/hydroxyapatite solution, 1.5 ml of 1% by volume glutaraldehyde was added and the obtained solution was placed on a magnetic stirrer for 3 h.

### 2.3.5 Fabricating Chi/TPP

To fabricate the bone scaffold sample, Chi/TPP was first dissolved in 0.05 g of low molecular weight chitosan powder in 5 ml of 1% by volume acetic acid (1 wt.% chitosan) and stirred magnetically for 2 min to obtain a clear gel. Then, 0.13 ml of 15 wt.% of sodium tripolyphosphate was added to the formed gel and the obtained solution was placed on a magnetic stirrer for 3 h.

### 2.3.6 Fabricating Chi/HA25%/TPP

To fabricate the Chi/HA25%/TPP bone scaffold sample, the first 0.15 g of low molecular weight chitosan powder was dissolved in 15 ml of 1% by volume acetic acid and placed on a magnetic stirrer for 2 min to obtain a clear gel. Then 0.05 g of hydroxyapatite synthesized by sol–gel method was dispersed in some deionized water and the suspension obtained by burette was added to chitosan gel. It was then stirred by a magnetic stirrer for 2 h to obtain a (3: 1 chitosan/hydroxyapatite solution). Then, 0.39 ml of 15 wt.% sodium triphosphate was added to the formed gel and the resulting solution was placed on a magnetic stirrer for 3 h. The rest of the samples (50% and 75%) were made in the same way with different percentages of hydroxyapatite.

Finally, eight samples were poured into dialysis filters for 24 h to remove acetic acid. The samples were then placed in an ultrasonic bath for 10 min to mix thoroughly and air bubbles were removed. In the next step, the samples were

poured into petri dishes and placed at  $-20\text{ }^{\circ}\text{C}$  for 24 h to be frozen. The frozen samples were placed in a freeze-drying apparatus for 48 h to remove the solvent and form the desired scaffolds as shown in Fig. 1.

## 2.4 Field Emission Scanning Electron Microscope (FESEM)

To study the structure and morphology, synthesized hydroxyapatite powder, chitosan, and scaffold samples were imaged by field emission scanning electron microscope. Due to the non-conductivity of the samples before analysis, the samples were coated with gold by sputtering. In this research, the Tescan MIRA3 device has been used.

## 2.5 X-Ray Diffraction Analysis (XRD)

X-ray diffraction analysis was used to detect fuzzy size and crystallinity. This analysis was performed by  $\text{Cu K}\alpha$  irradiation with conditions  $2\theta = 10\text{--}70$  degrees and a time interval of one second and a step distance of 0.02 degrees.

## 2.6 Fourier Transform Infrared (FTIR) Spectroscopy

To find out the chemical composition and type of bonds in the scaffold specimens, Fourier's infrared spectroscopy was performed by a Perkin-Elmer device in the range of  $500\text{--}3000\text{ cm}^{-1}$ .

## 2.7 Thermal Analysis (DTA-TG)

DTA-TG thermal analysis was used to investigate the thermal behavior of hydroxyapatite at  $80\text{ }^{\circ}\text{C}$ . This test was performed in the temperature range of 0 to  $1200\text{ }^{\circ}\text{C}$  and heating rate of  $10\text{ }^{\circ}\text{C}/\text{min}$ .

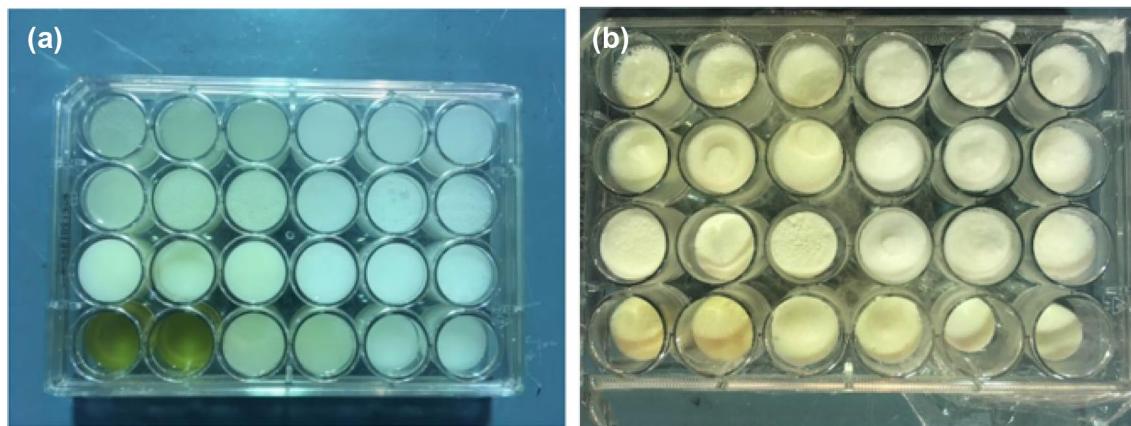


**Fig. 1** a Samples poured into 24 containers b Frozen samples at  $-20\text{ }^{\circ}\text{C}$

## 2.8 Investigation of Mechanical Properties

To investigate the mechanical properties of scaffold samples, uniaxial pressure test was selected. Cylindrical specimens with a diameter of 1 cm and a height of 2 cm were prepared in 24 molds, then tested by Hounsfield (H10KS).

## 2.9 Determination of Porosity Percentage

Eight samples of scaffolds were evaluated by Archimedes method to determine the porosity percentage. First, the dry weight of the scaffold was measured. The scaffolds were then placed in SBF for 48 h. The scaffolds were removed from the SBF, their saturation weight and immersion weight were measured. Applying density and porosity were calculated using two Eqs. 1 and 2.

$$\rho_R = \frac{\rho_w - m_1}{m_2 - m_3} \quad (1)$$

$$P_t = \frac{\rho - \rho_R}{\rho} \times 100 \quad (2)$$

where  $\rho_R$ ,  $\rho_w$ ,  $\rho$ ,  $m_1$ ,  $m_2$ ,  $m_3$ ,  $P_t$ , are the apparent density of the scaffold, density of SBF as a penetrant, composite density, dry weight of scaffolding, Scaffold weight with saturated liquid, Weight of scaffold immersed in liquid (weight of immersion), Percentage of porosity, respectively.

### 2.9.1 Investigation of Biological Behavior of Scaffolds

All samples with dimensions of 1 × 1 cm are cut, weighed and then immersed in a solution of distilled water and SBF

at 37 °C. Regularly dilute the solution until it reaches equilibrium and weighs after cleaning the surface water. Water absorption percentage was defined using Eq. 3 below.

$$\text{Swelling Ratio} = \frac{W_b - W_a}{W_a} \times 100 \quad (3)$$

where  $W_b$  and  $W_a$  are swollen and dry specimen weights, respectively.

## 3 Results and Discussion

### 3.1 Synthesized Hydroxyapatite Characterization Tests

DTA-TG thermal analysis was performed after the preparation of dried hydroxyapatite gel. Figure 2 shows DTA-TG thermal analysis tests of dried hydroxyapatite gel.

After calcination of dried hydroxyapatite at 700 °C, thermal analysis (STA) was performed. Figure 3 shows the thermal analysis (STA) of synthesized hydroxyapatite powder.

Thermal analysis of DTA – TG, HA gel dried at 80 °C is shown in Fig. 2. In the TG curve, a sharp drop in temperature of about 100 °C is observed due to the physical loss of adsorbed water molecules. Then the weight loss in the temperature range of 185–210 °C is related to the withdrawal of crystallized water and the disappearance of the nitrate and ammonia groups. The weight loss of about 450 °C is related to the crystallization of HA powder. After 500 °C, almost no weight loss is observed, which indicates the thermal stability of HA powder. In the DTA curve, an endothermic peak around 70 °C is observed, which is due to evaporation

**Fig. 2** Thermal behavior of hydroxyapatite gel

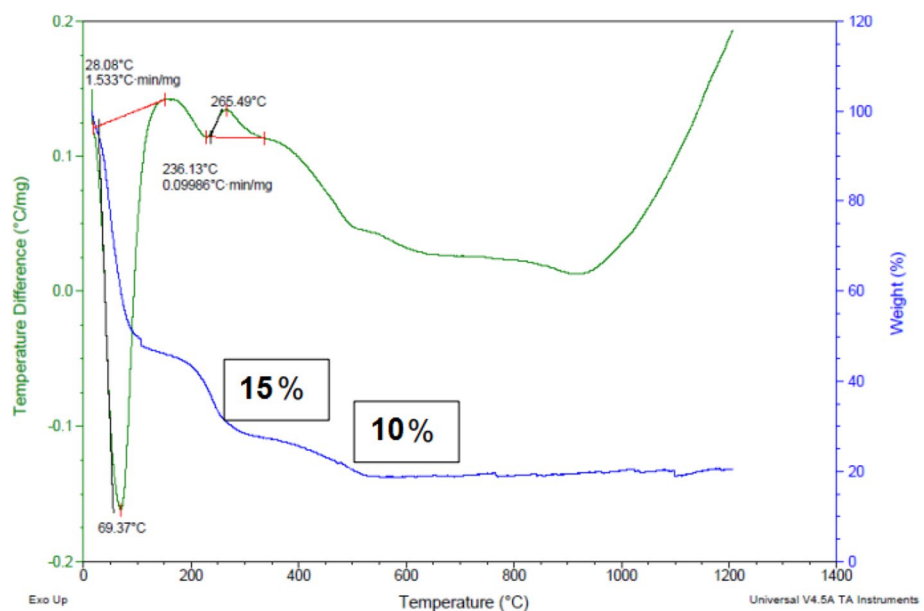
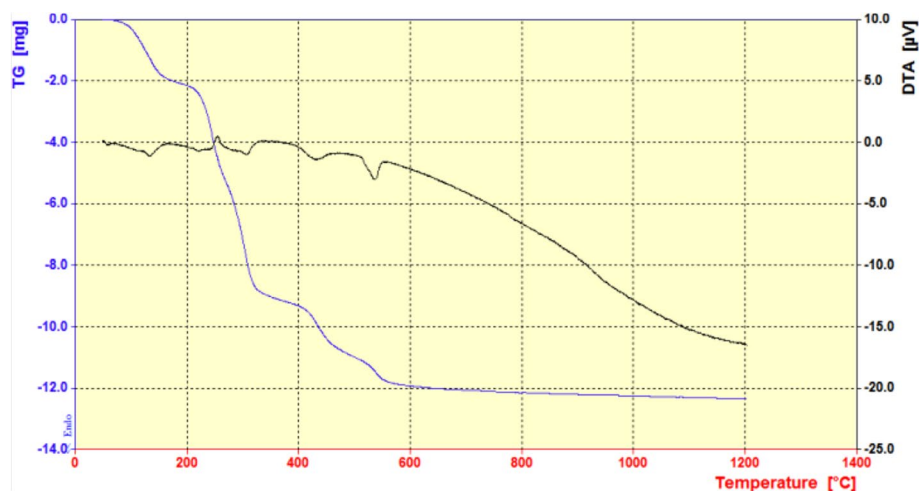


**Fig. 3** Thermal behavior (STA) of calcined HA at 700 °C



of water and absorbed moisture. In the DTA curve, a specific endothermic peak appears in the temperature range of 200–300 °C, which corresponds to a weight loss of about 15% wt. in the TG curve. Due to the presence of nitrate and ammonia groups in the dried gel, this weight loss is related to the removal of nitrate and ammonium groups from the gel. The temperature range of stability of ammonium nitrate is low and it is destroyed by heat treatment at higher temperatures. At these temperatures the formation of pure hydroxyapatite without additional materials can be expected. The DTA curve in the high temperature region up to approximately 900 °C does not show any significant change, which indicates the thermal stability of the hydroxyapatite phase. A weak exothermic peak at about 900 °C can be attributed to the decomposition of hydroxyapatite and the formation of tricalcium phosphate. Finally, the dried hydroxyapatite gel is calcined at 700 °C and the thermal analysis (STA) is as shown in Fig. 3.

### 3.2 X-Ray Diffraction Analysis Results (XRD)

The X-ray diffraction pattern of hydroxyapatite particles was analyzed by Xpert software and standard card to confirm the accuracy of the synthesized material. Figure 4 shows the XRD pattern of the synthesized material. As shown in Fig. 4, there is a relatively good agreement between the synthesized sample and the JCPDS card peaks regarding the location of the peaks with the diffraction pattern and the diffraction intensity. The XRD pattern of the synthesized hydroxyapatite was indexed as a hexagonal structure, which is incredibly near to the values in the literature (JCPDS No. 96–900–3549). In HA synthesis, some amounts of beta-tricalcium phosphate and calcium phosphate phases are formed as impurities. They will show themselves in the diffraction pattern in the form of peaks in the main field. If the amount of these impurities increases, the peaks become

more significant and more evident in the diffraction pattern. In Fig. 4, the beta-tricalcium phosphate and calcium phosphate (JCPDS No. 96–900–5866) is compared with the peaks obtained from the synthesized hydroxyapatite, which shows the high purity of the synthesized hydroxyapatite.

The crystallite size of synthesized hydroxyapatite nanoparticles was estimated and reported in Table 4.

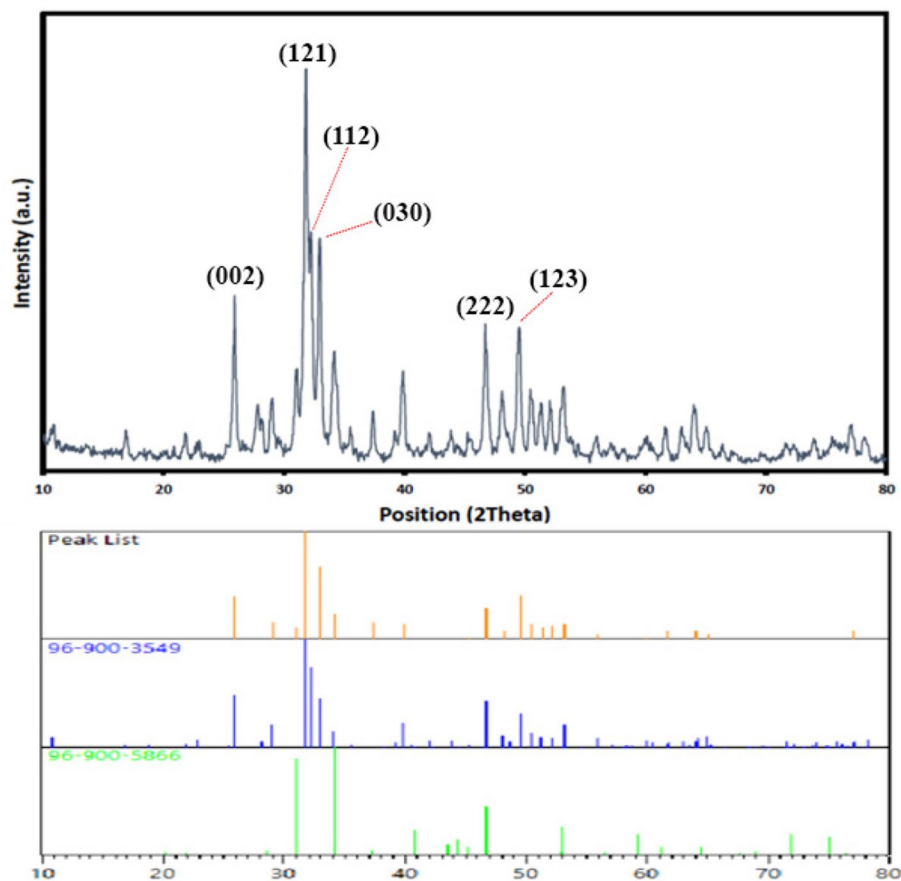
### 3.3 Field Emission Scanning Electron Microscopy Results (FESEM)

FESEM images were used to evaluate the morphology, uniformity, and particle size of HA. Figure 5 shows FESEM images of synthesized hydroxyapatite powder and Merck. Figure 5a, which shows the image of the synthesized powder along with its approximate particle size, that shows the particle size well. Therefore, based on these images, it can be claimed that the synthesized HA is also morphologically validated, and the synthesis process has led to the achievement of a nanostructured powder. Figure 5b shows SEM image of Merck hydroxyapatite powder. As can be seen in this figure, the structure and morphology of hydroxyapatite particles synthesized by the sol–gel method are very close to Merck hydroxyapatite particles.

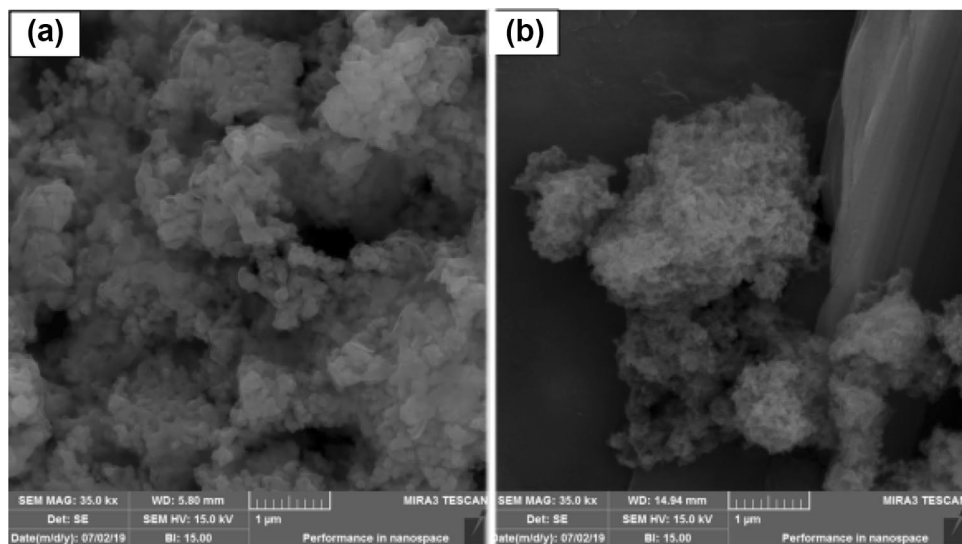
### 3.4 Scaffolding Specification Tests

To study the morphology, structure, and uniformity of scaffold samples, they were imaged by field scanning electron microscopy. Figure 6 shows FESEM images of a Chi/GA scaffold sample at different magnifications.

Figures 6a and b show that in the Chi/GA scaffold specimen the shape and distribution of porosity are uniform. The shape of the pores is due to the release of solvent during freeze-drying. The thickness of the polymer layer is about 0.37 μm. Figure 6c also shows the uniform presence of

**Fig. 4** XRD analysis of synthesized HA powder**Table 4** The peak position, full width at half maximum ( $\beta$   $\frac{1}{2}$ ), and calculated crystal size for nanoparticles

h k l	(002)	(121)	(112)	(030)	(222)	(123)
Peak position $2\theta$ ( $^{\circ}$ )	25.87	31.76	32.19	32.90	46.69	49.48
FWHM $\beta$ ( $^{\circ}$ )	0.25	0.37	0.38	0.25	0.37	0.37
Size (nm)	34.05	23.32	22.73	34.61	24.42	24.69
$\lambda=0.154$ nm, $K=0.94$						

**Fig. 5 a** Synthesized hydroxyapatite powder **b** FESEM image of MERCK HA powder

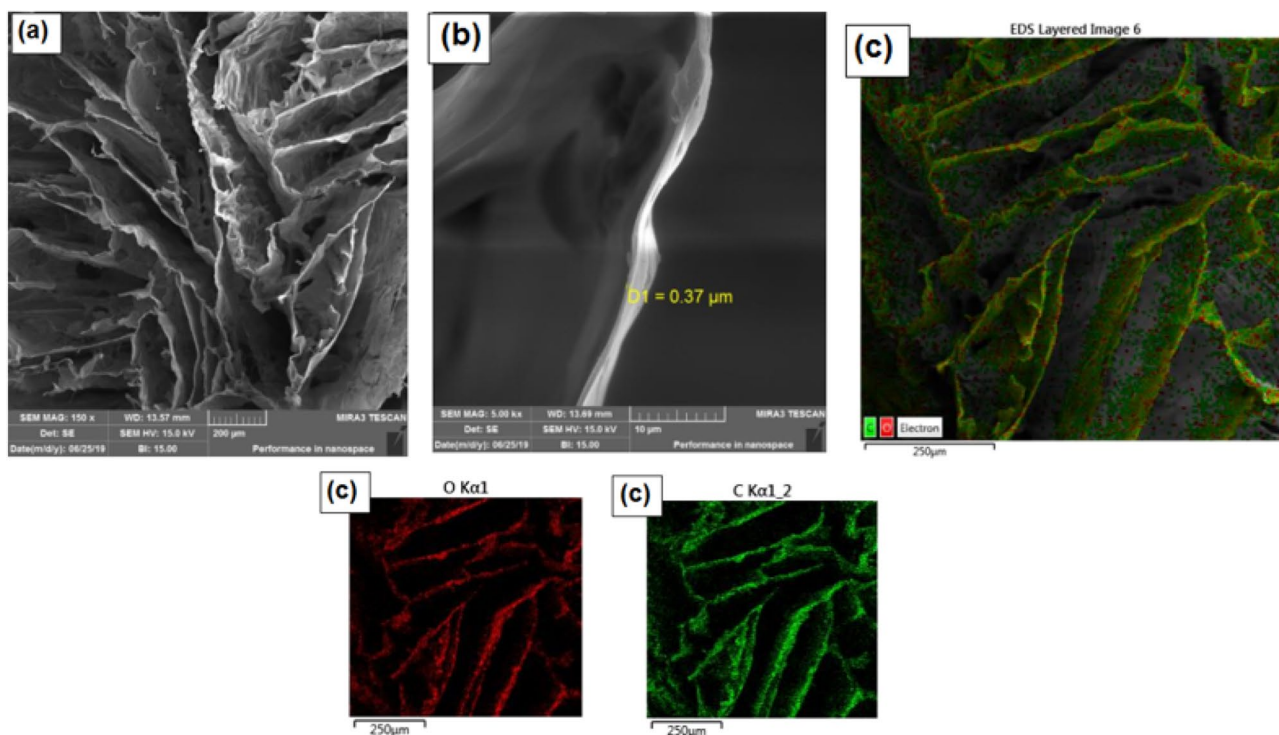


**Fig. 6** FESEM images of the CHI/GA scaffold sample (a) 200 magnification (b) 10 magnification and (c) MAPPING

chitosan and glutaraldehyde in the scaffold. Figure 7 shows FESEM of a Chi/HA25%/GA scaffold sample at different magnifications.

As shown in Fig. 7, the porosity size in the Chi/HA25%/GA sample increased compared to the Chi/GA sample. Chitosan layers appear to have deteriorated in some areas. Figure 8 shows FESEM images of a Chi/HA50%/GA scaffold sample at different magnifications.

As can be seen in Figs. 8a, b, the size of the pores is smaller than the previous two samples, probably due to the higher amount of hydroxyapatite. Figure 9 shows FESEM images of a Chi/HA75%/GA scaffold sample at different magnifications.

Figure 9 shows the perfectly uniform distribution of hydroxyapatite particles in the chitosan field. As can be seen, the amount of hydroxyapatite is higher than the previous two samples. The size of the pores has decreased. Also, the porosities do not seem to be the way to go and their distribution is uniform.

### 3.5 Results of Fourier Transform Infrared Spectroscopy (FTIR)

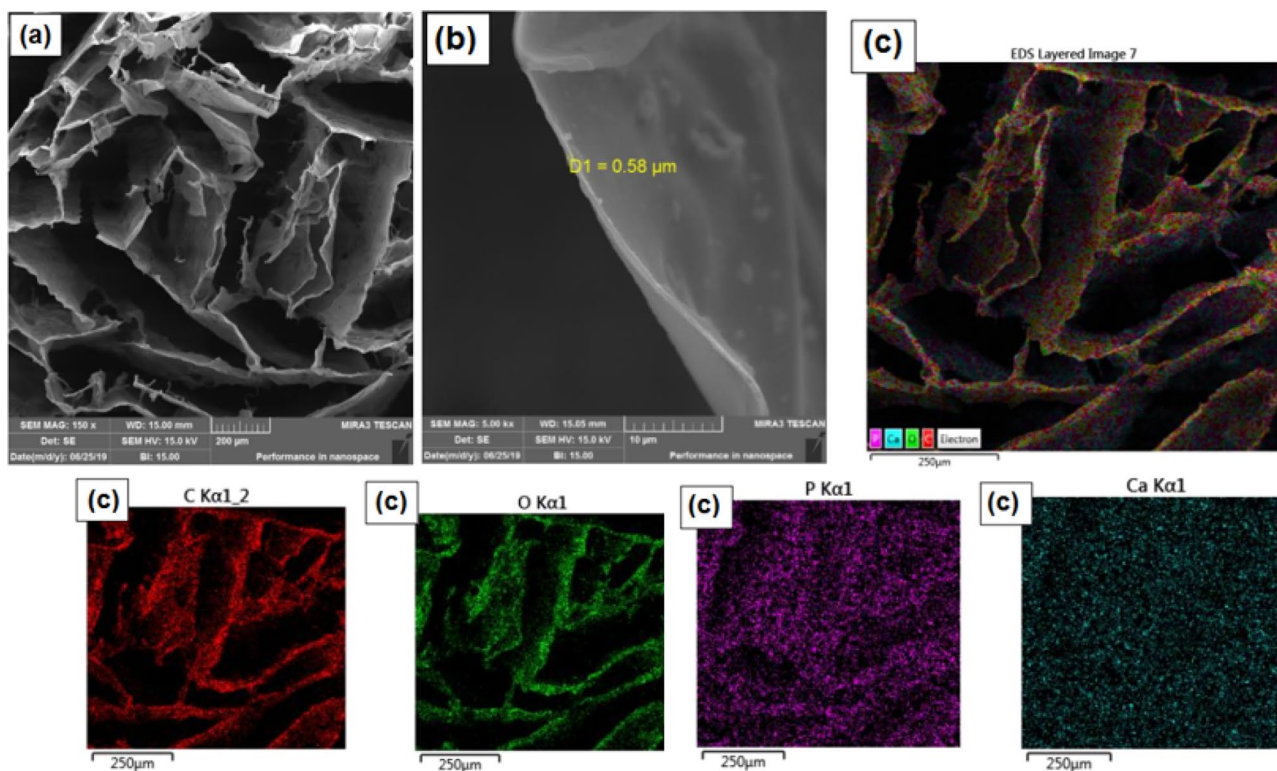
Figure 10 shows Fourier transform infrared spectroscopy analysis of Chi/GA, Chi/HA25%/GA, Chi /HA50%/GA, Chi /HA75%/GA scaffold samples. Also, Fig. 11 shows the

molecular structure of chitosan polymer with glutaraldehyde (GA) molecules as a cross-linker.

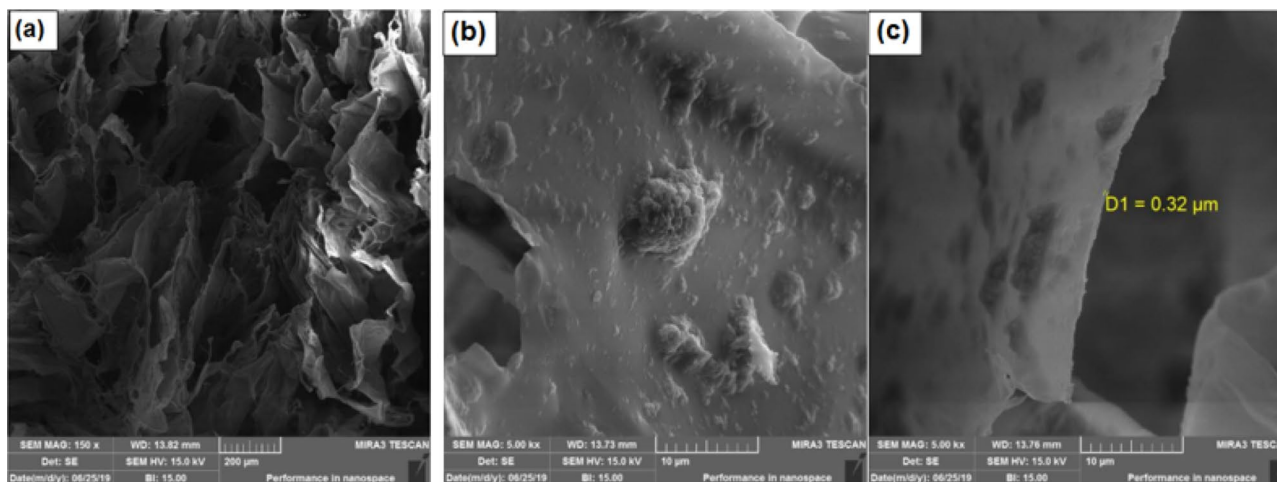
The adsorption peak around  $3366\text{ cm}^{-1}$  is related to the O–H bonds of Chitosan. The presence of hydroxy functional groups in the structure of Chitosan causes intermolecular hydrogen bonding in the synthesized composite structure. These intermolecular hydrogen bonds strengthen the composite structure. Also, hydroxyl functional groups in the composite structure cause hydrogen bonding between chitosan and hydroxyapatite molecules (Fig. 11). The peaks at  $2866\text{ cm}^{-1}$  correspond to the stretching vibration of the aliphatic C–H bonds. The signal that appeared at  $1640\text{ cm}^{-1}$  corresponds to the stretching vibration of imine bonds. Observations of imine bond peaks demonstrate the reaction between chitosan and glutaraldehyde molecules, which causes a cross-linking between chitosan molecules. The peak at approximately  $1552\text{ cm}^{-1}$  is related to the bending vibrations of N–H bonds. The peak at  $1407\text{ cm}^{-1}$  corresponds to bending vibrational  $\text{CH}_2$  bonds of Chitosan and GA. The adsorption peaks observed in  $1023$  and  $629\text{ cm}^{-1}$  belong to the phosphate group correspond to the stretching vibration of P=O and P–O bonds, respectively.

Figure 12 shows Fourier transform infrared spectroscopy analysis of Chi/TPP, Chi/HA25%/TPP, Chi /HA50%/TPP, Chi /HA75%/TPP scaffold samples. Also, Fig. 13 shows the molecular structure of chitosan polymer with Sodium triphosphate (TPP) molecules as a cross-linker.





**Fig. 7** FESEM images of the CHI/HA25%/GA scaffold sample (a) 200 magnification (b) 10 magnification and (c) MAPPING

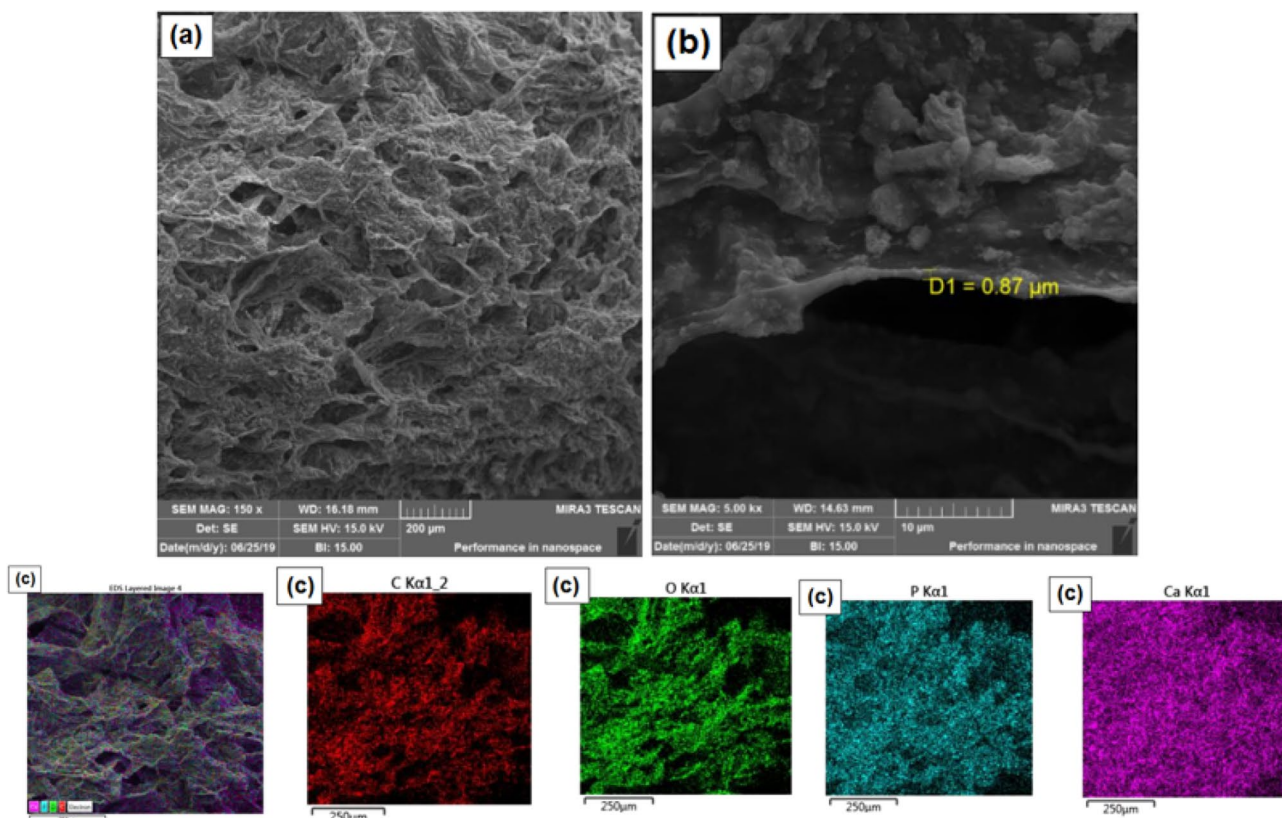


**Fig. 8** FESEM images of the CHI/HA50%/GA scaffold sample (a) 200  $\mu\text{m}$  magnification (b) Hydroxyapatite particles in the chitosan field (c) 10  $\mu\text{m}$  magnification

The peak intensity in the  $1410\text{ cm}^{-1}$  area decreases as the weight percentage of hydroxyapatite increases. This peak is related to the bending vibrational bonds of  $\text{CH}_2$  in the structure of Chitosan. In TPP cross-linking samples, the displacement of peaks belonging to OH and NH groups at 3,500 is more severe than in GA cross-linking samples.

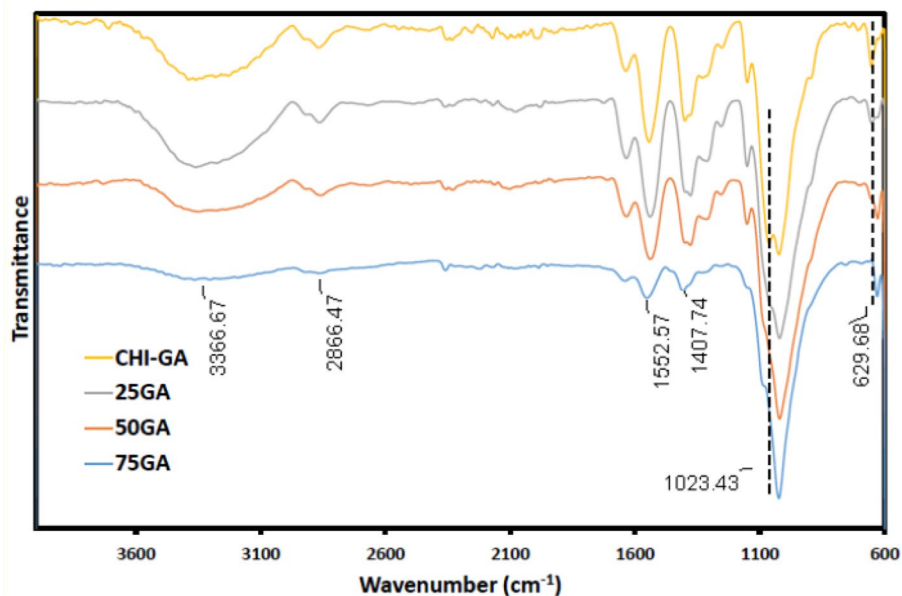
### 3.6 Results of Energy-Dispersive X-Ray Spectroscopy (EDS)

Figure 14 shows EDS analysis of Chi/GA, Chi/HA25%/GA, Chi/HA50%/GA, Chi/HA75%/GA, Chi/TPP, Chi/HA25%/TPP, Chi/HA50%/TPP, Chi/HA75%/TPP scaffold



**Fig. 9** FESEM images of the CHI/HA75%/GA scaffold sample (a) 200 magnification (b) 10 magnification and (c) MAPPING

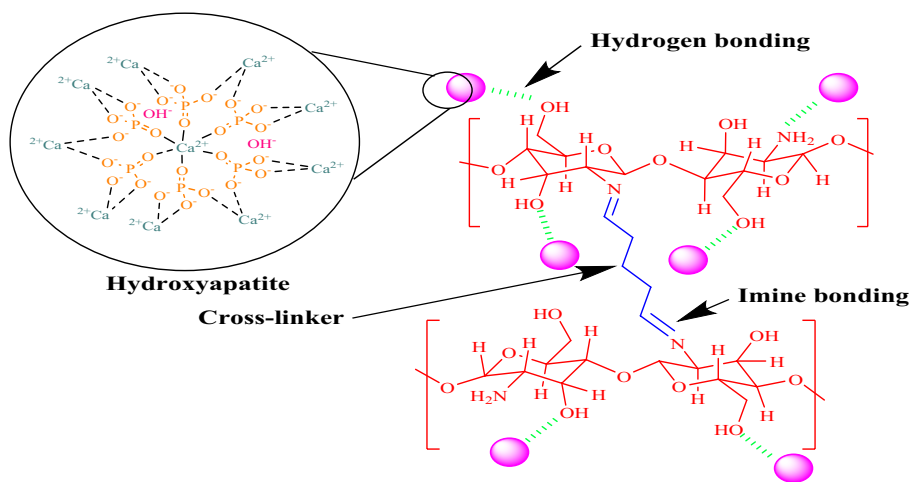
**Fig. 10** FT-IR of Chi/GA, Chi/HA25%/GA, Chi/HA50%/GA, Chi/HA75%/GA scaffold samples



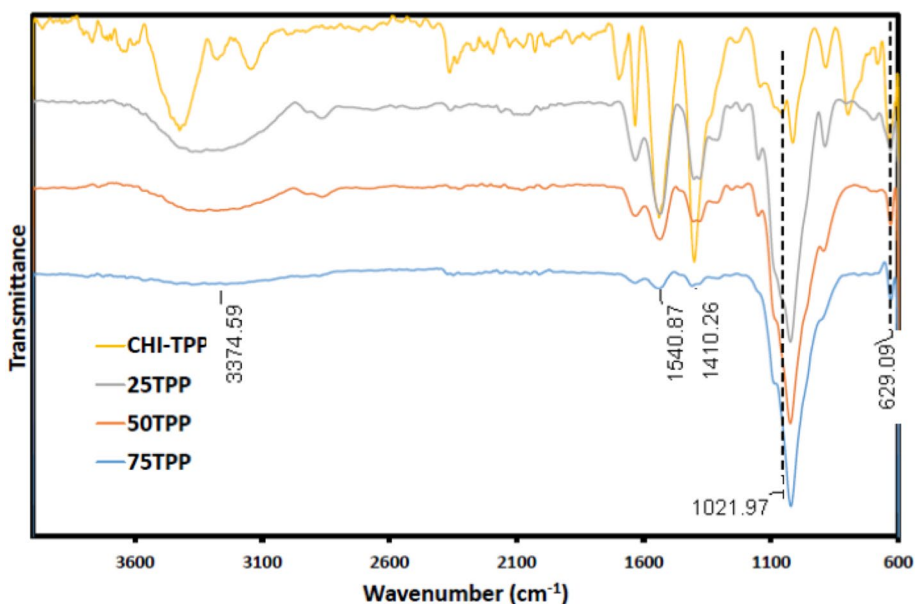
samples. The stoichiometric HA has a Ca: P weight ratio of 2.151. This ratio is 2.11, 2.37, 1.90 and 2.33 for Chi/HA25%/GA, Chi/HA75%/GA, Chi/HA50%/TPP and Chi/HA75%/TPP, respectively. This ratio is 2.82 and 1.28 for Chi/HA50%/GA and Chi/HA25%/TPP, respectively. These

values indicate the presence of impurities in the structure. This is an advantage due to the lack of calcium in HA in normal bone tissue in the samples Chi/HA25%/GA, Chi/HA25%/TPP and Chi/HA50%/TPP. In addition, the carbon seen in this diagram can be attributed to chitosan,

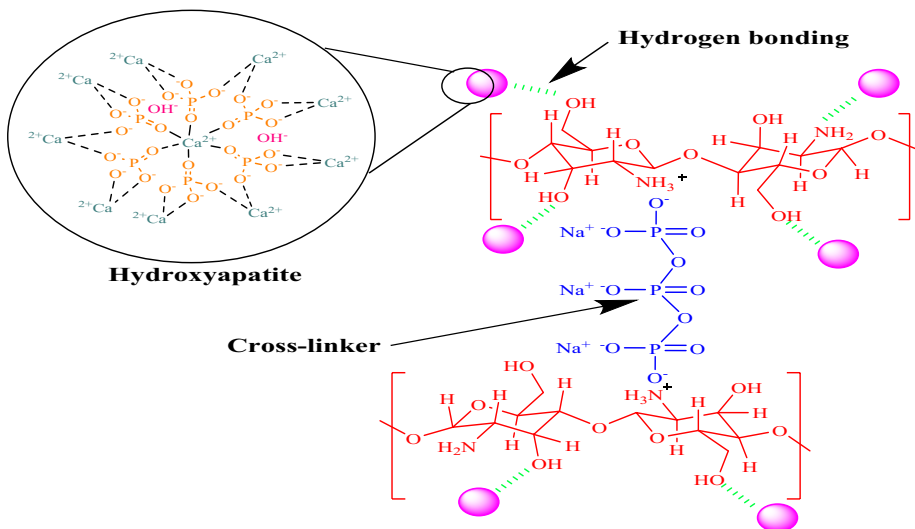
**Fig. 11** Molecular structure of Chi /HA/GA composite

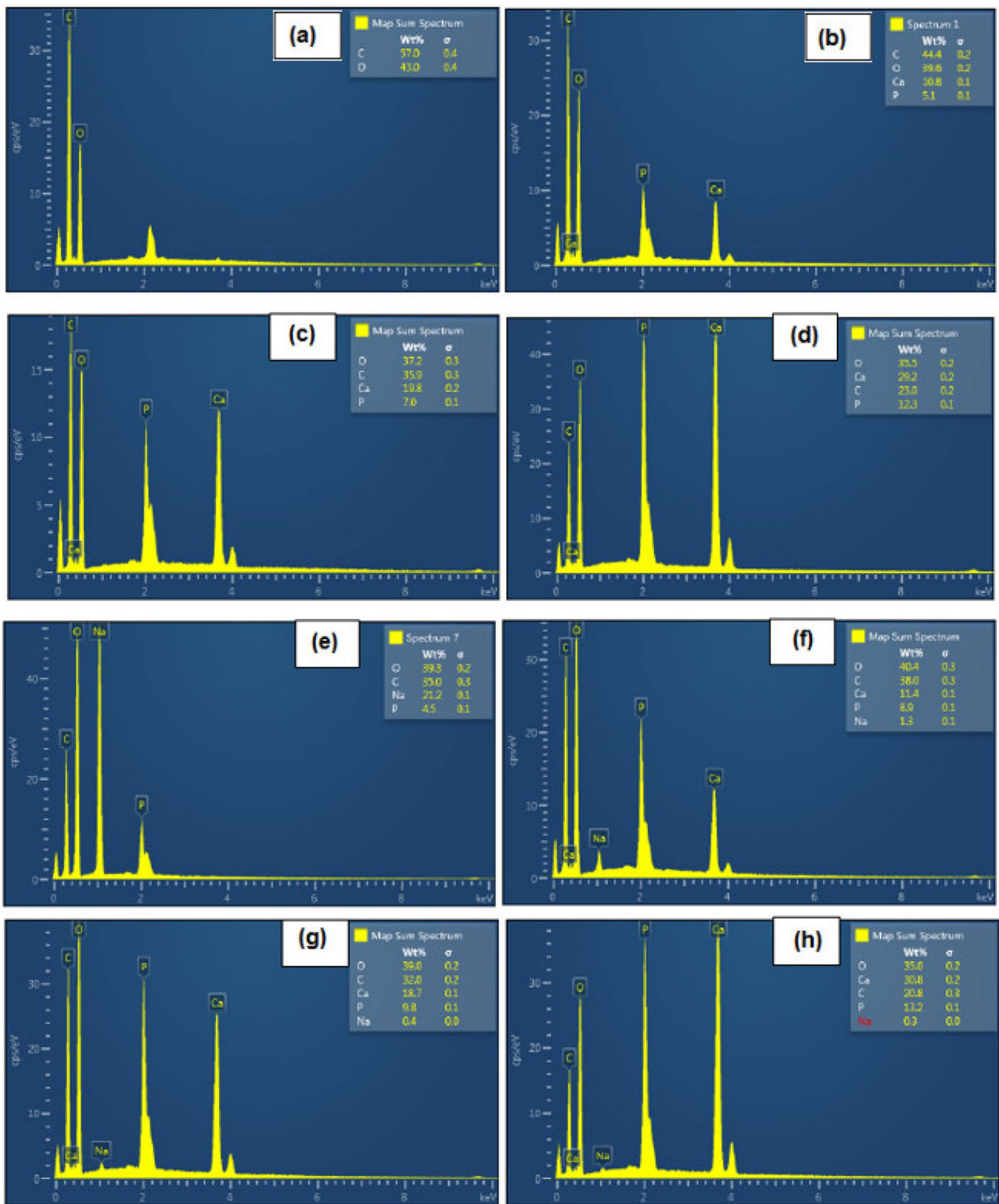


**Fig. 12** FT-IR of Chi/TPP, Chi/HA25%/TPP, Chi /HA50%/TPP, Chi /HA75%/TPP scaffold samples



**Fig. 13** Molecular structure of Chi /HA/TPP composite

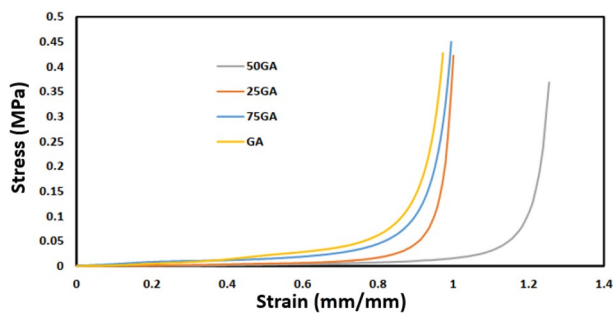




**Fig. 14** EDS analysis of (a) Chi/GA, (b) Chi/HA25%/GA, (c) Chi/HA50%/GA, (d) Chi/HA75%/GA, (e) Chi/TPP, (f) Chi/HA25%/TPP, (g) Chi/HA50%/TPP, (h) Chi/HA75%/TPP

**Table 5** Compressive strength of scaffold specimens

Specimen	Compressive strength (MPa)
Chi/GA	0.061568
Chi/HA25%/GA	0.01675
Chi/HA50%/GA	0.07215
Chi/HA75%/GA	0.044139
Chi/HA25%/TPP	0.025465
Chi/HA50%/TPP	0.07243
Chi/HA75%/TPP	0.028436

**Fig. 15** Stress–strain curves for samples Chi/GA, Chi/HA25%/GA, Chi/HA50%/GA, Chi/HA75%/GA

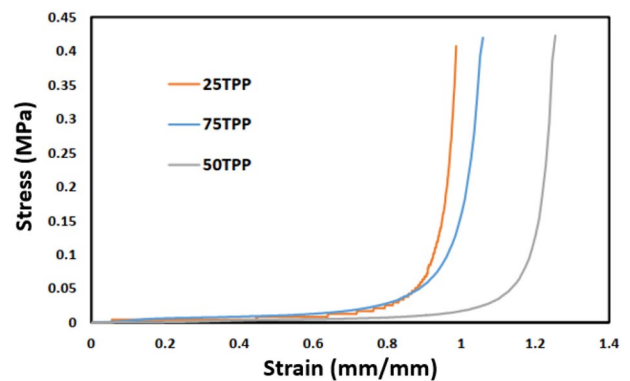
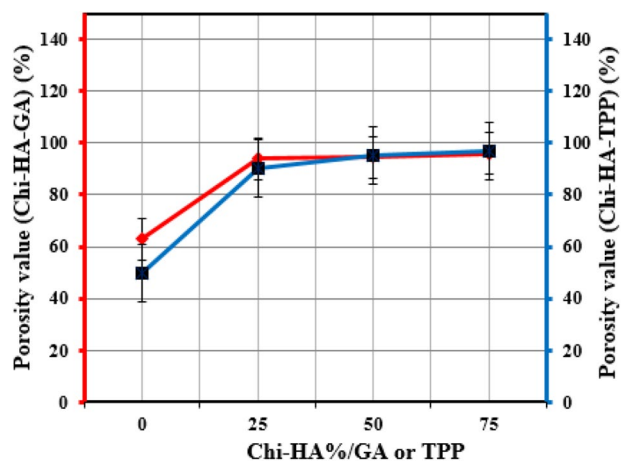
glutaraldehyde or the presence of carbonate in the structure of hydroxyapatite. Sodium in Chi/HA25%/TPP, Chi/HA50%/TPP and Chi/HA75%/TPP is also due to the presence of sodium triphosphate crosslinker.

### 3.7 Investigation of Mechanical Properties

From each of the polymer and composite samples with 25, 50 and 75 wt.% of HA, three samples were evaluated by uniaxial pressure test. By adding 75 wt.% of HA to the polymer matrix, we saw a 28.3% decrease in compressive strength at 0.8 strain as shown in Table 5.

In terms of strength, a sample containing 75 wt.% of hydroxyapatite has the lowest strength loss. If we compare the samples in terms of length change, the samples Chi/HA50%/GA and Chi/HA50%/TPP showed the best behavior. Therefore depending on the application, we can use the Chi/HA75%/GA sample which has high strength, or the Chi/HA50%/GA and Chi/HA50%/TPP samples which have better elongation. Figure 15 shows the stress curves in terms of engineering strain for the samples Chi/GA, Chi/HA25%/GA, Chi/HA50%/GA, Chi/HA75%/GA.

Figure 16 shows the stress curves in terms of engineering strain for the samples Chi/HA25%/TPP, Chi/HA50%/TPP, Chi/HA75%/TPP.

**Fig. 16** Stress–strain curves for samples Chi/HA25%/TPP, Chi/HA50%/TPP, Chi/HA75%/TPP**Fig. 17** porosity of prepared scaffolding

### 3.8 Determination of Porosity Percentage

The results obtained in Fig. 17 show that scaffolds with a porosity of about 90% have been prepared. Further porosity facilitates the bone formation and accelerates the healing of damaged bone. Due to the high porosity percentage, we are expected to see suitable biological properties.

### 3.9 Results of Biological Analysis

After immersing the scaffolds in SBF solution for 1 week as shown in Fig. 18, three analyzes were performed by SEM and EDS to evaluate their biological behavior, especially their bioactivity.

The results of swelling ratio of specimens that immersed in a solution of distilled water and SBF at 37 °C are shown in Fig. 19.

The results of this category of evaluations can be seen in the images in Fig. 20. In SEM images, germination and

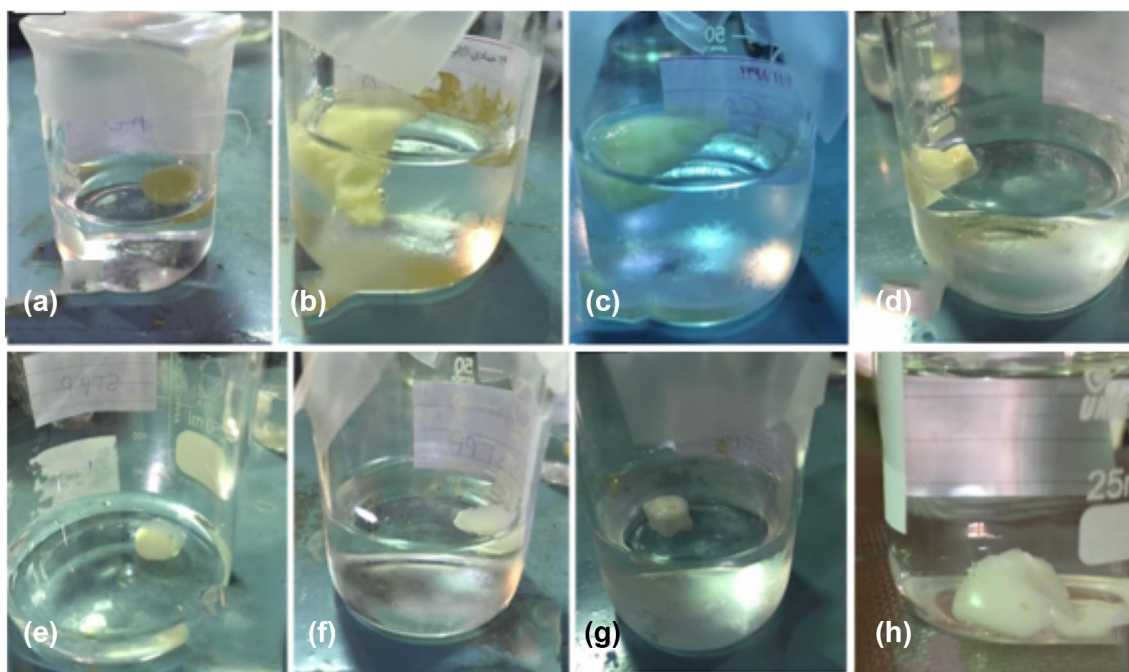


**Fig. 18** All samples in SBF solution (a) Chi/GA, (b) Chi/HA25%/GA, (c) Chi/HA50%/GA, (d) Chi/HA75%/GA, (e) Chi/GA, (f) Chi/HA25%/TPP, (g) Chi/HA50%/TPP, (h) Chi/HA75%/TPP

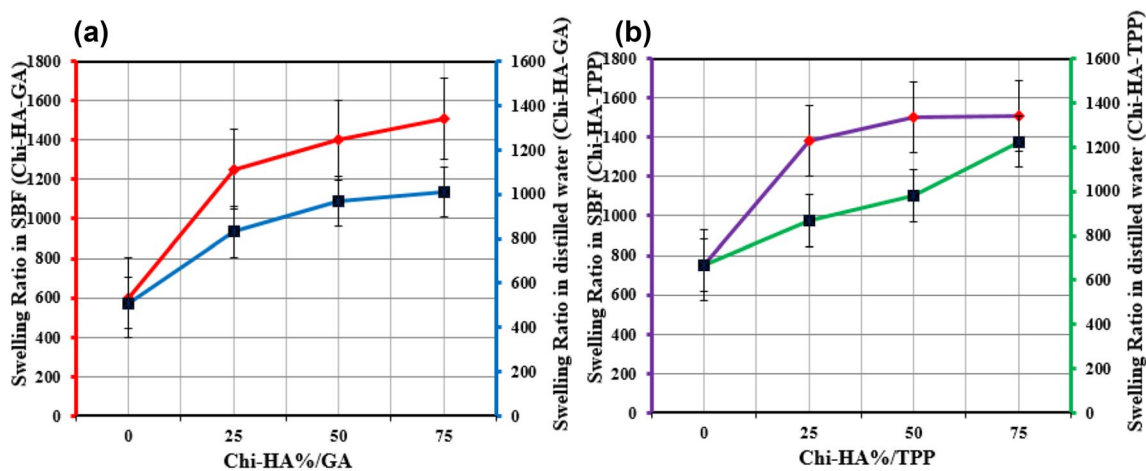


**Fig. 19** Swelling ratio of: (a) Chi/GA, Chi/HA25%/GA, Chi/HA50%/GA, and Chi/HA75%/GA in distilled water and SBF, Swelling ratio of: (b) Chi/TPP, Chi/HA25%/TPP, Chi/HA50%/TPP, and Chi/HA75%/TPP in distilled water and SBF

growth of a homogeneous phase can be seen on the scaffold. After 1 week of immersion, a layer of calcium phosphate is formed on the scaffold, which is micron thick.

In the first stage, by adsorption of  $H_3O^{3+}$ ,  $OH^-$  groups are formed on the surface of the scaffold. For this purpose, a number of positive ions on the surface of the scaffold must be removed. As a result, the surface of the scaffold has a negative charge.  $Ca^{2+}$  ions from SBF then settle on the scaffold, resulting in the formation of calcium hydroxide.

Therefore, the surface charge potential is positive and the conditions for  $H_3PO_3^-$  ion deposition are provided so that the surface charge becomes negative and amorphous calcium phosphate is formed. By continuing these steps, amorphous calcium phosphate is formed on the surfaces in contact with SBF liquid. Therefore, more apatite is deposited on composites containing 75% hydroxyapatite, and the particle formed on this composite scaffold is smaller than the particles formed on the chitosan scaffold, which is due to the

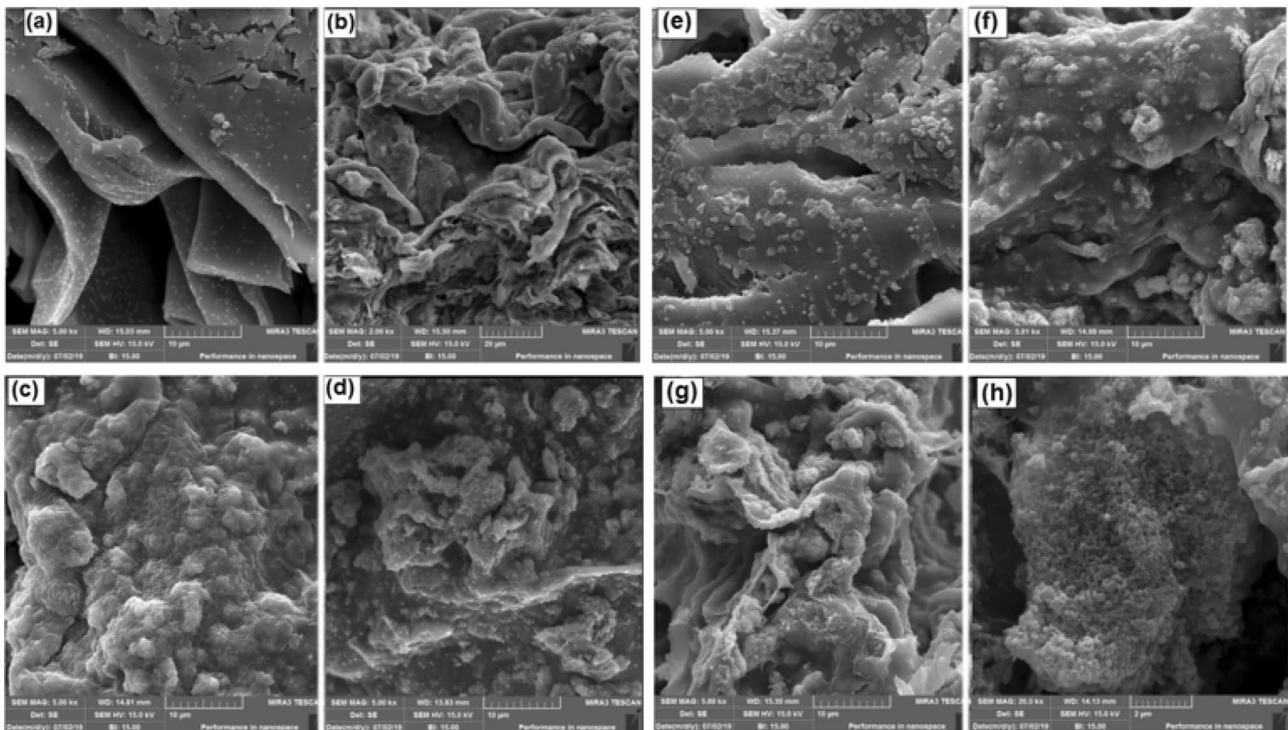


**Fig. 20** SEM of (a) Chi/GA, (b) Chi/HA25%/GA, (c) Chi/HA50%/GA, (d) Chi/HA75%/GA, (e) Chi/TPP, (f) Chi/HA25%/TPP, (g) Chi/HA50%/TPP, (h) Chi/HA75%/TPP after leaving SBF

limited inorganic ions that make the mineral have limited places for germination.

## 4 Conclusion

In this study, hydroxyapatite was synthesized by sol–gel method and eight samples of composite scaffolds with different weight percentages of hydroxyapatite and different crosslinkers were made, the important results of which are as follows:

- Hydroxyapatite synthesized by sol–gel method has a nanometer structure close to the powder purchased from Merck.
- Eight scaffolding specimens have a porosity of more than 90% and as the amount of hydroxyapatite increases, the size of the pores decreases and the scaffolding becomes denser.
- Further porosity facilitates the bone formation and accelerates the healing of damaged bone. Due to the high porosity percentage, we are expected to see suitable biological properties.
- According to the FTIR results, the cross-linkers of TPP and GA performed well and, in addition to work-

ing well on chitosan, formed hydrogen bonds between hydroxyapatite and chitosan.

- According to SEM images, biocompatibility of samples increases with increasing hydroxyapatite content.
- The samples Chi/HA50%/GA and Chi/HA50%/TPP showed the best behavior at mechanical properties. Therefore depending on the application, we can use the Chi/HA75%/GA sample which has high strength,
- The samples of Chi/HA50%/GA and Chi/HA50%/TPP had better elongation.

**Acknowledgements** We are thankful to the Iranian Nanotechnology Development Committee for their support.

**Author Contributions** AF wrote the whole of article and analyzed mechanical, thermal, and biological properties. AHG analyzed FT-IR, XRD, EDS, and MAPPING. Both authors discussed the results, reviewed, and approved the final version of the manuscript.

**Funding** All experiments were performed on a personal budget.

**Data Availability** Data required to reproduce these findings have been given in the text.

## Declarations

**Conflict of Interest** No conflict of interest exists in the submission of this article.

**Ethical Approval** Not applicable.

**Consent to Participate** Not applicable.

**Consent to Publication** The article is approved by all authors for publication.

## References

1. A. Farazin, F. Aghadavoudi, M. Motifard, S. Saber-Samandari, A. Khandan, *J. Appl. Comput. Mech.* **7**, 1907 (2021)
2. A. Farazin, H.A. Aghdam, M. Motifard, F. Aghadavoudi, A. Kordjamshidi, S. Saber-Samandari, S. Esmaili, A. Khandan, *J. Nanoanalysis* **6**, 172–3 (2019)
3. Z.S. Kazeroni, M. Telloo, A. Farazin, S. Saber-Samandari, E. Sheikhabaehi, B. Kamyab-Moghadas, H. JoneidiYekta, S. Esmaili, A. Khandan, *AUT J. Mech. Eng.* **5**, 109 (2021)
4. A. Farazin, M. Mohammadimehr, *Int. J. Adv. Manuf. Technol.* **118**, 103 (2022)
5. A. Farazin, A. Khan, *J. Strain Anal. Eng. Des.* (2021). <https://doi.org/10.1177/03093247211043714>
6. A. Farazin, Z. Torkpour, S. Dehghani, R. Mohammadi, M.D. Fahmy, S. Saber-Samandari, K.A. Labib, A. Khandan, *Int. J. Basic Sci. Med.* **6**, 44 (2021)
7. D. Green, D. Walsh, S. Mann, R.O.C. Oreffo, *Bone* **30**, 810 (2002)
8. A.B. Yeatts, J.P. Fisher, *Bone* **48**, 171 (2011)
9. M. Giner, E. Chicardi, A.F. Costa, L. Santana, M.Á. Vázquez-Gómez, C. García-Garrido, M.A. Colmenero, F.J. Olmo-Montes, Y. Torres, M.J. Montoya-García, *Metals (Basel)*. **11**, 130 (2021)
10. J.J. Andrew, V. Arumugam, C. Santulli, *Compos. Struct.* **143**, 63 (2016)
11. S. Gowid, E. Mahdi, S.S. Youssef, E. Moustafa, A. Mosleh, A. Shokry, *Compos. Struct.* **276**, 114569 (2021)
12. C. Kang, Z. Liu, B. Shirinzadeh, H. Zhou, Y. Shi, T. Yu, P. Zhao, *Compos. Struct.* **267**, 113861 (2021)
13. Q. Wu, Q. Wang, S. Ren, L. Zu, Q. Zhang, G. Zhang, *Compos. Struct.* **259**, 113455 (2021)
14. L. Zu, H. Xu, B. Zhang, D. Li, B. Zi, *Compos. Struct.* **194**, 119 (2018)
15. K. Moreno, J. García-Miranda, C. Hernández-Navarro, F. Ruiz-Guillén, L. Aguilera-Camacho, R. Lesso, A. Arizmendi-Morquero, *J. Compos. Mater.* **49**, 1345 (2015)
16. M.P. Bernardo, B.C.R. da Silva, L.H.C. Mattoso, *J. Compos. Mater.* **55**, 2289 (2021)
17. A.M. Deliormanli, *J. Compos. Mater.* **50**, 917 (2016)
18. A. Asuvaran and G. Elatharasan, *Silicon* (2021).
19. K. Vishal, K. Rajkumar, P. Sabarinathan, and V. Dhinakaran, *Silicon* (2022).
20. G. Anand and S. Vishvanathperumal, *Silicon* (2022).
21. P. Vimala, L. L. Krishna, and S. S. Sharma, *Silicon* (2022).
22. R. Srinivasan, M. Kamaraj, D. Rajeev, S. Ravi, and N. Senthilku-mar, *Silicon* (2022).
23. H. Idrees, S.Z.J. Zaidi, A. Sabir, R.U. Khan, X. Zhang, S. Hassan, *Nanomaterials* **10**, 1970 (2020)
24. B.I. Oladapo, S.A. Zahedi, S.O. Ismail, D.B. Olowade, *Renew. Sustain. Energy Rev.* **150**, 111505 (2021)
25. Q. Yang, J. Peng, H. Xiao, X. Xu, Z. Qian, *Carbohydr. Polym.* **278**, 118952 (2022)
26. N. Castro, S. Ribeiro, M.M. Fernandes, C. Ribeiro, V. Cardoso, V. Correia, R. Minguez, S. Lanceros-Mendez, *Adv. Biosyst.* **4**, 2000125 (2020)
27. D.T. Fox, D.E. Soltis, P.S. Soltis, T.-L. Ashman, Y. Van de Peer, *Trends Cell Biol.* **30**, 688 (2020)
28. N. Mehrban, C.P. Molina, L.M. Quijano, J. Bowen, S.A. Johnson, J. Bartolacci, J.T. Chang, D.A. Scott, D.N. Woolfson, M.A. Birchall, S.F. Badylak, *Acta Biomater.* **111**, 141 (2020)
29. Z. Wang, Y. Wang, J. Yan, K. Zhang, F. Lin, L. Xiang, L. Deng, Z. Guan, W. Cui, H. Zhang, *Adv. Drug Deliv. Rev.* **174**, 504 (2021)
30. A.Z. Kharazi, M. Fathi, F. Bahmani, H. Fanian, *J. Compos. Mater.* **46**, 2753 (2012)
31. M.L. Chinta, A. Velidandi, N.P.P. Pabbathi, S. Dahariya, S.R. Parcha, *Int. J. Biol. Macromol.* **175**, 495 (2021)
32. P. Feng, J. Jia, M. Liu, S. Peng, Z. Zhao, C. Shuai, *Mater. Des.* **210**, 110066 (2021)
33. X. Wang, Y. Li, J. Wei, K. de Groot, *Biomaterials* **23**, 4787 (2002)
34. D.-M. Liu, Q. Yang, T. Troczynski, W.J. Tseng, *Biomaterials* **23**, 1679 (2002)
35. S.J. Kalita, *Functional nanostructures* (Springer, New York, 2008), pp. 168–219
36. H.K. Varma, S.N. Kalkura, R. Sivakumar, *Ceram. Int.* **24**, 467 (1998)
37. W.-J. Shih, Y.-F. Chen, M.-C. Wang, M.-H. Hon, *J. Cryst. Growth* **270**, 211 (2004)
38. M. F. Favatela, J. Otarola, V. B. Ayala-Peña, G. Dolcini, S. Perez, A. Torres Nicolini, V. A. Alvarez, and V. L. Lassalle, *J. Inorg. Organomet. Polym. Mater.* (2022).
39. M. A. Gabal, E. A. Al-Harthy, Y. M. Al Angari, A. Awad, A. A. Al-Juaid, M. A. Hussein, A. M. Abdel-Daiem, T. R. Sobahi, and A. Saeed, *J. Inorg. Organomet. Polym. Mater.* (2022).
40. H.H. Refai, A.A. Ganash, M.A. Hussein, *J. Inorg. Organomet. Polym. Mater.* **32**, 713 (2022)
41. K. Chinnaiyah, T. Theivashanthi, K. Kannan, M.S. Revathy, V. Maik, H. Parangusan, S.C. Jeyaseelan, K. Gurushankar, *J. Inorg. Organomet. Polym. Mater.* **32**, 583 (2022)
42. Ş Duman, B. Bulut, *Ceram. Int.* **47**, 13912 (2021)
43. A. Farazin, S. Sahmani, M. Soleimani, A. Kolooshani, S. Saber-Samandari, A. Khandan, *Ceram. Int.* **47**, 18339 (2021)
44. J. Dorazilová, J. Muchová, K. Šmerková, S. Kočiová, P. Diviš, P. Kopel, R. Veselý, V. Pavlíňáková, V. Adam, L. Vojtová, *Nanomaterials* **10**, 1971 (2020)
45. S. Zhang, J. Li, J. Li, N. Du, D. Li, F. Li, J. Man, *RSC Adv.* **10**, 34308 (2020)
46. A. Farazin, M. Mohammadimehr, A.H. Ghasemi, H. Naeimi, *RSC Adv.* **11**, 32775 (2021)

**Publisher's Note** Springer Nature remains neutral with regard to jurisdictional claims in published maps and institutional affiliations.